

ChemComm

Chemical Communications

Accepted Manuscript

This article can be cited before page numbers have been issued, to do this please use: P. Sanwal, Y. Zhang, A. Raza and G. Li, *Chem. Commun.*, 2024, DOI: 10.1039/D4CC02722A.



This is an Accepted Manuscript, which has been through the Royal Society of Chemistry peer review process and has been accepted for publication.

Accepted Manuscripts are published online shortly after acceptance, before technical editing, formatting and proof reading. Using this free service, authors can make their results available to the community, in citable form, before we publish the edited article. We will replace this Accepted Manuscript with the edited and formatted Advance Article as soon as it is available.

You can find more information about Accepted Manuscripts in the [Information for Authors](#).

Please note that technical editing may introduce minor changes to the text and/or graphics, which may alter content. The journal's standard [Terms & Conditions](#) and the [Ethical guidelines](#) still apply. In no event shall the Royal Society of Chemistry be held responsible for any errors or omissions in this Accepted Manuscript or any consequences arising from the use of any information it contains.

Transition Metal Oxide Clusters: Advanced Electrocatalysts for a Sustainable Energy Future

 Sanwal Piracha,^{‡,ab} Yifei Zhang,^{‡,ab} Ali Raza,^c and Gao Li^{*ab}

 Received 00th January 20xx,
Accepted 00th January 20xx

DOI: 10.1039/x0xx00000x

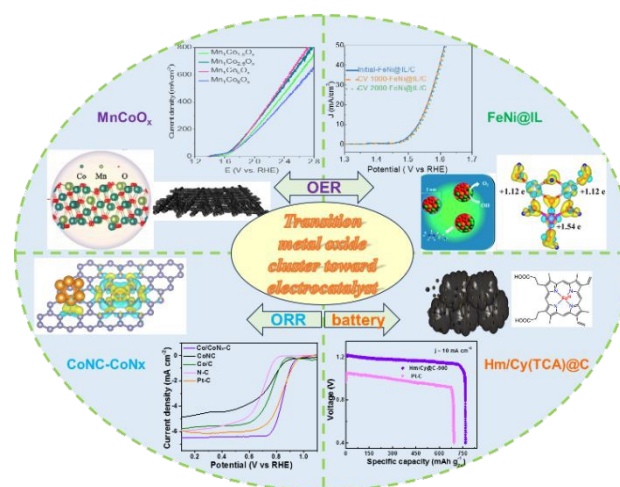
www.rsc.org/

The comprehensive utilization of sustainable green energy is essential to face the global energy and environmental crisis. The oxygen reduction reaction (ORR), oxygen evolution of hydrogen (OER), and electrocatalytic urea synthesis (EUS) are the pivotal electrocatalytic processes, necessitating the development of low-cost electrocatalysts with high efficiency. The small-sized transition metal oxide (TMO) clusters have attracted a lot of attention because of their exceptional qualities, such as exhibiting a dense array of low-coordinated metal active sites (e.g. abundant metal cation defects and oxygen vacancy), amorphous structures with high surface energy, high atom utilization efficiency, and cost-effectiveness. Furthermore, the synergistic actions between metal clusters and TM-N_x single atom actives remarkably boost up the electrocatalytic performances, corroborated by density functional theory (DFT). More efforts in this comprehensive feature article are expected to achieve insights into the fundamental understanding of electrocatalytic reaction mechanisms in our lab and serve as a guide for creating cutting-edge electrocatalysts of transition metal oxide clusters.

Introduction

Due to expanding global energy use and growing environmental concerns, there is a growing demand for clean, sustainable energy technologies including fuel cells, solar cells, and metal-air batteries.¹⁻⁴ The efficiency of catalysts is crucial for the application of these technologies, which rely on catalytic processes, including the oxygen reduction reaction (ORR), the oxygen evolution of hydrogen (OER), and electrocatalytic urea synthesis (EUS) from nitrate ion and CO₂.⁵⁻⁷ The high price, lack of stability, and restricted availability of traditional noble metal catalysts like Ir, Pd, and Pt prevent their broad use as energy solutions.⁵⁻⁷ To overcome these obstacles and make renewable energy systems more practical, lots of efforts have gone into creating catalysts that don't include metals or Pt yet are just as efficient for ORR, OER, EUS, and other processes.⁸⁻¹⁰ Multifunctional electrocatalysts as substitutions, which have recently been developed, may provide several methods simultaneously, opening up new possibilities for integrated energy conversion systems.¹¹⁻¹³ There is an alternative for improving electrochemical activity with less expense and resource consumption thanks to new catalysts, such as ultrasmall-sized particles (also named clusters, size of 2-5 nm). Incorporating sophisticated catalysts into comprehensive

electrochemical systems may greatly improve energy conversion's lifespan and efficiency, propelling us toward a greener, more sustainable energy future.^{5, 14-17}



Scheme 1 The outline of this articles on metal oxide clusters, including acidic/alkaline OER and alkaline ORR and zinc-air battery.

Transition metal oxide (TMO) clusters (particle size of 3-6 nm) have a dense array of low-coordinated metal active sites (e.g. abundant metal cation defects and oxygen vacancy), amorphous structures with high surface energy due to the distorted TM-O bonds, high atom utilization efficiency, cost-effectiveness, a few to name.¹⁸⁻²¹ These unique geometric characteristics are conducive to electrochemical activity by providing metal-metal contacts and reaction intermediate adsorption sites.^{10, 22, 23} TMO clusters may break scaling relations by lowering reaction barriers, regulating the rate-determining step (RDS) in electrocatalysis

^a Institute of Catalysis for Energy and Environment, College of Chemistry and Chemical Engineering, Shenyang Normal University, Shenyang 110034, Liaoning, China

^b State Key Laboratory of Catalysis, Dalian Institute of Chemical Physics, Chinese Academy of Sciences, Dalian 116023, China, E-mail: gaoli@dicp.ac.cn (G.L.).

^c Department of Physics "Ettore Pancini", University of Naples Federico II, Piazzale Tecchio, 80, 80125 Naples, Italy.

^d ‡ P.S. and Y.Z. contributed equally to this work.



and improving catalytic performances (including activity and selectivity) in ORR, OER, EUS, etc. Their ability to create catalysts with co-adsorbates, promoters, ligands, and new alloy structures makes them ideal options for electrocatalysis and energy conversion technology.²⁴⁻²⁶ Because of the expensive nature and limited geological resources of precious group metal (PGM) electrocatalysts such as RuO_2 and IrO_2 , there has been growing interest in PGM-free catalysts.²⁷⁻²⁹ Therefore, catalysts based on transition metals that are common on Earth (such as Ni, Co, Fe, Mn, etc.), particularly transition metal hydroxides (TMH), have attracted interest due to their electrocatalytic activity, affordability, and strong durability as effective and economical alternatives. In recent decades, several³⁰⁻³² TM sulfides,³³⁻³⁵ nitrides,³⁶ phosphides,^{30,32} oxides,^{37,38} and hydroxides^{39,40} have been explored as promising alternative OER electrocatalysts. And earth-abundant TMHs have attracted attention as promising OER electrocatalysts due to their activity, low cost, excellent stability, and environmentally friendly nature.⁴¹ The Fe-based NNMEs have exceptional ORR catalytic activity. These comprise a high concentration of iron-based species such as oxides (Fe_xO_y), nitrides (FeN_x), carbides (FeC_x), and sulfides (FeS_x).⁴²⁻⁴⁶ Species with high electronegativity can attach stable FeNC electrocatalyst active sites. This might potentially modify the adsorption and desorption of O intermediate on the core Fe atoms, affecting the activities of the oxygen reduction reaction (ORR).⁴⁷⁻⁴⁹

According to the advances of TM composites, our group's research in this article recently explores novel approaches to increase catalytic efficiency in various applications, such as the creation of intrinsically stable MnCoO_x solid solutions for long-term water oxidation, the impact of many active sites on

promotion in Fe-based ORR electrocatalysts, the cooperative role of cobalt clusters- CoN_x composites in enhancing electrochemical-oxygen-reduction, and synergistic effect of Fe clusters and FeN_x for electrocatalytic urea synthesis (EUS) from nitrate and CO_2 , Scheme 1. Furthermore, the effective electrocatalytic characteristics of ultrafine metallic hydroxide nanoparticles and FeNi hydroxide nanoclusters modified by ionic liquids for oxygen evolution processes are emphasized. Additionally, the use of atomically precise metal nanoclusters for active-site engineering in heterogeneous catalysis is investigated, offering insights into customizing catalytic processes for increased efficiency. What's more, the mechanism of all these electrocatalysis is well revealed by experiments combined with theoretical calculations. These results highlight the significance of material design, synthesis techniques, and active-site modification in developing electrocatalysts for sustainable energy systems. This joint effort shows encouraging directions for creating robust and effective electrocatalytic systems necessary to meet urgent global energy issues. Lastly, we provide our thoughts about upcoming initiatives to create efficient TM electrocatalysts.

Synthetic Methods

Pechini method

Pechini process is a sol-gel route invented by Maggio Pechini in that suitable metal oxides or salts are chelated with hydroxycarboxylic acid (e.g. citric acid) in aqueous solutions and then reacted with glycol to form large, cross-linked polymeric networks at 150–250 °C, which are eventually charred and achieves small-sized metal oxide solid

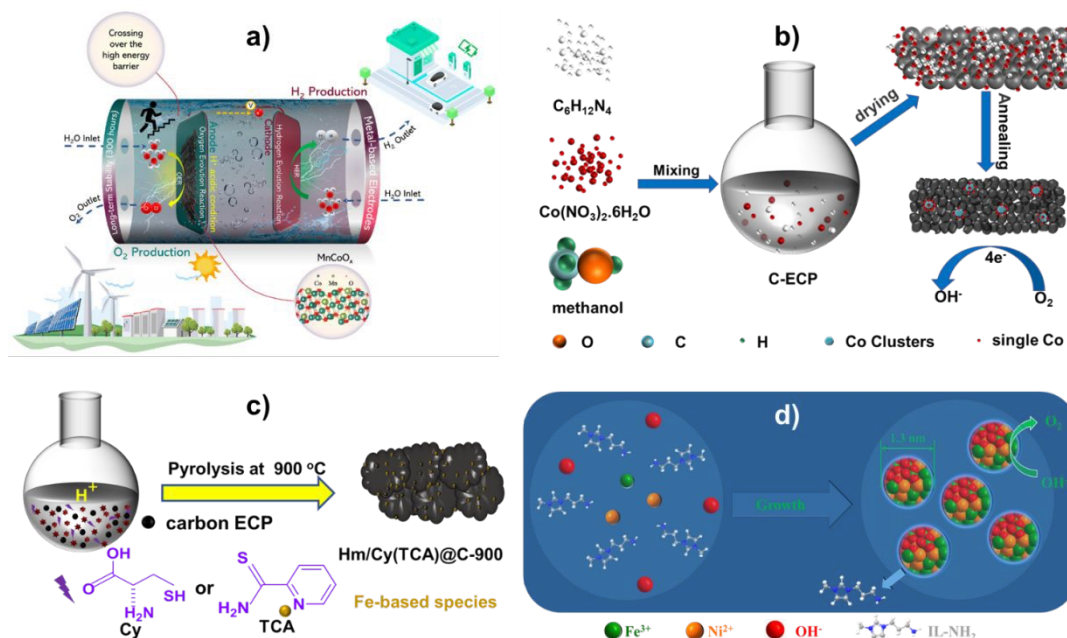


Figure 1. (a) Visual representation of the OER process in acidic environments, elucidating the critical points of this investigation. Reproduced with permission from ref. ⁵², Copyright 2023 Royal Society of Chemistry. (b) The synthesis of Co/CoN_x-C. Reproduced with permission from ref. ⁵³, Copyright 2022 Royal Society of Chemistry. (c) An illustrated method for producing electrocatalysts using Hm/Cy@C-900 and Hm/TCA@C-900. Redrawn from ref. ⁵⁷, Copyright 2023 Royal Society of Chemistry. (d) Producing amorphous FeNi hydroxide clusters capped with IL. Redrawn from ref. ⁵⁶, Copyright 2020 Royal Society of Chemistry.



solutions at temperatures of 300–350 °C^{50,51}. For example, using the potassium permanganate redox technique, the author researched printing CoMnO_x compounds on carbon paper (CP). $\text{Mn}_1\text{Co}_5\text{O}_x$ produced in research differs significantly from doped compounds. Potassium permanganate oxidizes low-valent cobalt to high-valent. In doing so, a uniform solid solution of $\text{Mn}_1\text{Co}_5\text{O}_x$ is formed. a Mn-rich doped Co_3O_4 . The solid solution crystal structure's capacity to maintain the solvent's crystal structure, resulting in the same material, structure, and characteristics, is fascinating⁵¹. This single-phase solid solution has excellent OER catalytic activity. The $\text{Mn}_1\text{Co}_5\text{O}_x$ catalyst performed well in acid electrolytes, achieving overpotentials of 275 $\text{mV}@10 \text{ mA cm}^{-2}$ and 569 $\text{mV}@100 \text{ mA cm}^{-2}$. Additionally, MnCoO_x showed exceptional stability of catalysis for 300 hours at 100 mA cm^{-2} , indicating its potential for electrocatalytic applications. As indicated in (Figure 1a), MnCoO_x 's strong OER catalytic efficiency in an acidic medium. In addition, it highlights this material's unique design and excellent OER performance⁵². DFT results manifested that the Mn dopant can significantly elevate the d-band of Co_3O_4 (-2.05 eV) to near Fermi level (-1.78 eV) and sharply reduce the overpotential of OER from 2.79 eV ($\text{Co}_3\text{O}_4(311)$) to 0.82 eV ($\text{MnCoO}_x(311)$). Thus, the Mn dopant and Ov can stabilize OER intermediates and then reduce the energy barrier of OER and improve catalytic activity.

Further, Zhang et al.⁵³ developed a straightforward process for mass-producing cobalt-based electrocatalysts by carbonizing at 500 °C shown in (Figure 1b). STEM and X-ray absorption showed pyrolytic treatment merged metallic Co clusters with CoN_x sites. In oxygen electroreduction operations, the $\text{Co/CoN}_x\text{-C}$ composite performed better than the commercial Pt/C catalyst, with an onset potential of 0.926 V vs. RHE and a half-wave potential $E_{1/2}$ of 0.853 V. The enhanced ORR performance of the $\text{Co/CoN}_x\text{-C}$ electrocatalyst is supported by first-principles calculations because of the special integration and ideal synergistic effects of electro-catalytically active CoN_x and Co cluster species.⁵⁴⁻⁵⁶ Theoretical results show that the cooperative Co clusters and CoN_x has higher electron density compared to bare Co/C and $\text{CoN}_x\text{-C}$ near Fermi level, thus, $\text{Co/CoN}_x\text{-C}$ exhibits the better conduct electricity. And the RDS over $\text{Co/CoN}_x\text{-C}$ and $\text{CoN}_x\text{-C}$ occurs at the first step of $\text{O}_2 \rightarrow \text{OOH}^*$, and that for Co/C is the last step of $\text{OH}^* \rightarrow \text{H}_2\text{O}$. Hence, the superior ORR activity of $\text{Co/CoN}_x\text{-C}$ catalysts is attributed to the unique integration and synergistic effect of metallic Co clusters and CoN_x species.

Single-step pyrolysis approach

The electrocatalysts were made using a straightforward one-pot method. The N and S precursors, Cy or TCA, were dissolved in an HNO_3 solution, and hemin was dissolved in a KOH solution. After that, the alkaline solution and the acidic solution were mixed for thirty minutes using ultrasonic shock. There was additional carbon ECP. An overnight drying process at 80 °C was used to eliminate all of the water following a three-hour reaction in a rotary evaporator. Pyrolysis was used to create the electrocatalysts at various temperatures in an argon environment. This was accomplished by using the identical synthesis procedure as for Hm/Cy@C but replacing Cy with TCA.⁵⁷ Notably, producing over 1 g of Fe-based electrocatalysts on a large scale is straightforward (Figure 1c). M@IL -modified amorphous metallic hydroxide nanoparticles are produced in a single process (Figure 1d). A IL-NH_2 methanol solution was mixed with an aqueous

solution of a metal-containing precursor, such as $\text{Fe}(\text{NO}_3)_3$, $\text{Co}(\text{NO}_3)_2$, or $\text{Ni}(\text{NO}_3)_2$, or their combination. Then, while the combination of methanol and water was being vigorously shaken, a NaOH aqueous solution was added. Vulcan XC-72R carbon powder was then added to the M@IL colloidal solution.⁵⁶

Mechanistic Insights into Electrocatalytic Activity in OER/ORR and Fuel Cell and Battery Applications

ORR

The Co clusters immobilized on N-doped carbon matrixes having a size that is around typical $4.4 \pm 1.2 \text{ nm}$ is shown in the STEM image of $\text{Co/CoN}_x\text{-C}$ (Figure 2a). As seen in Figure 2b, red cycles for CoN_x species and single Co atoms envelop metallic Co clusters. Single-Co-atoms (e.g., CoN_x species) firmly encircled the metallic Co clusters in N-doped carbon matrixes, according to the elemental mappings of $\text{Co/CoN}_x\text{-C}$ on a typical region of a STEM picture (Figure 2c). The Co K-edge X-ray absorption near-edge structure (XANES) of $\text{Co/CoN}_x\text{-C}$ is between Co foil and CoO_x , unlike conventional samples like Co foil, CoO, Co_3O_4 , and CoPc, Figure 2e. XANES peak of 7,726 eV in $\text{Co/CoN}_x\text{-C}$ reduced from 7,733 eV in Co foil, perhaps due to strong Co cluster- CoN_x interaction. Additionally, Fourier-transformed extended X-ray absorption fine structure (FT-EXAFS) analysis revealed a peak at 2.18 Å in $\text{Co/CoN}_x\text{-C}$ electrocatalyst

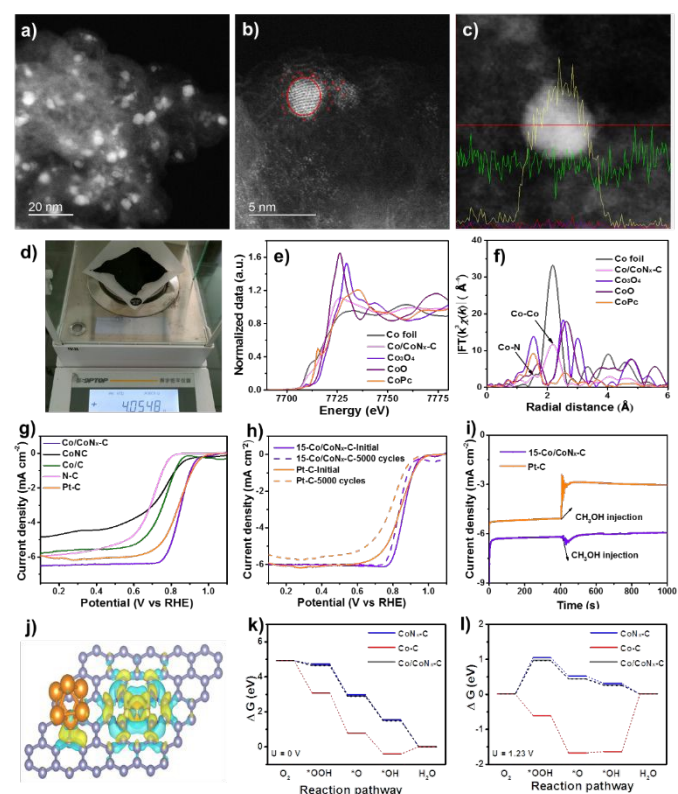


Figure 2 (a-c) S/TEM profiles with line scanning of $\text{Co/CoN}_x\text{-C}$. (d) Quality in one-pot synthesis. (e) FT-EXAFS and (f) normalized K-edge XANES spectra. (g) LSV curves. (h) LSV curves before and after 5000 cycles. (i) I-t responses of Pt/C and $\text{Co/CoN}_x\text{-C}$ after 400s of methanol addition. (j) DFT structure. (k,l) Diagram of free energy for ORR. Reproduced from reference⁵³, Copyright 2023 Royal Society of Chemistry.



(Figure 2f), indicating Co⁰-Co⁰ bonds and metallic Co clusters. XAS, XPS, and STEM strongly showed that the Co/CoN_x-C electrocatalyst's intimate integration of CoN_x species and Co clusters may synergistically boost ORR catalytic activity.⁵³

The Co/CoN_x-C ORR's catalytically active sites were discovered and identified by analyzing further cobalt-based electrocatalysts of Co/C and CoNC under identical ORR circumstances (Figure 2g). In terms of E_{1/2} comparison, ORR activity went as follows: Co/CoN_x-C > Co/C > CoNC > N-C. Co species increase ORR activity; the N-C deficient Co species exhibited the lowest ORR activity.⁵⁸ CoNC had a low restricted current density, suggesting that carbon support improves electrical conductivity. In an O₂-saturated 0.1 M KOH solution, Co/CoN_x-C was compared to commercial Pt/C for durability. Electrocatalyst LSV curves (Figure 2h) were analyzed after 5000 cycles at 100 mV s⁻¹. E_{1/2} losses were ~ 18 mV for Co/CoN_x-C and 47 mV for Pt/C, indicating the catalyst's stability and robustness. A possible explanation for the slight reduction in catalytic activity might be the partial formation of Co clusters (5.0±1.5 nm) in the spent Co/CoN_x-C catalyst. The I-t chronoamperometry in Figure 2i shows that Co/CoN_x-C's current density is relatively steady following methanol injection in an O₂-saturated 0.1 M KOH solution, demonstrating a higher resistance to methanol toxicity. The methanol oxidation process (MOR) over the Pt/C catalyst causes the current density to fluctuate following methanol input. CoNC had a low restricted current density, suggesting that carbon support improves electrical conductivity. In the control studies, Co/CoN_x-C ORR activity reduced considerably following acid leaching, which

preferentially eliminated metallic Co clusters from the electrocatalyst. Because of the optimal Co/CoN_x-C composition of 15 wt%, which promotes excellent dispersion of Co species and the cooperative effects of CoN_x sites and Co clusters, the ORR performance is improved.⁵⁹⁻⁶²

Integration of Co clusters with CoN_x-C in Co/CoN_x-C greatly improves stability. The charge density difference indicates several electron clouds surrounding CoN_x species and Co clusters (Figure 2j), indicating substantial electron exchange interaction. Co clusters and CoN_x species in Co/CoN_x-C transmitted 0.35 and 0.96 e, respectively, using the Bader charge calculation; these values are higher than 0.32 and 0.87 in Co/C and CoN_x-C. The electrocatalytic activity was increased by the interaction and impact of symbiotic Co clusters and CoN_x species in Co/CoN_x-C. The steps that determine a rate for Co/CoN_x-C and CoN_x-C occur in the first phase (O₂ → OOH*), with energy barriers of 0.18 eV and 0.26 eV (U = 0 V), according to the ORR process depicted in Figure 2k, l. Endothermic water generation results from RDS over Co/C in the last step (OH* → H₂O). Three Co sites were assessed for the CoN₄ and Co cluster sites because of the Co/CoN_x-C's strong ORR performance.⁶³

NNME nanomaterials are potential ORR electrocatalysts.^{56, 64-68} However, the costly and complicated synthetic process will impede NNME expansion. Hemin (Hm) develops ORR-efficient carbon-supported FeN_x electrocatalysts⁶⁹⁻⁷¹. Iron nitride and sulfide in Hm/Cy@C-900 are confirmed by the overlapping signals of N, S, and Fe species. The different capacities of the N and S-containing functional groups in the Cy and TCA ligands to coordinate could be

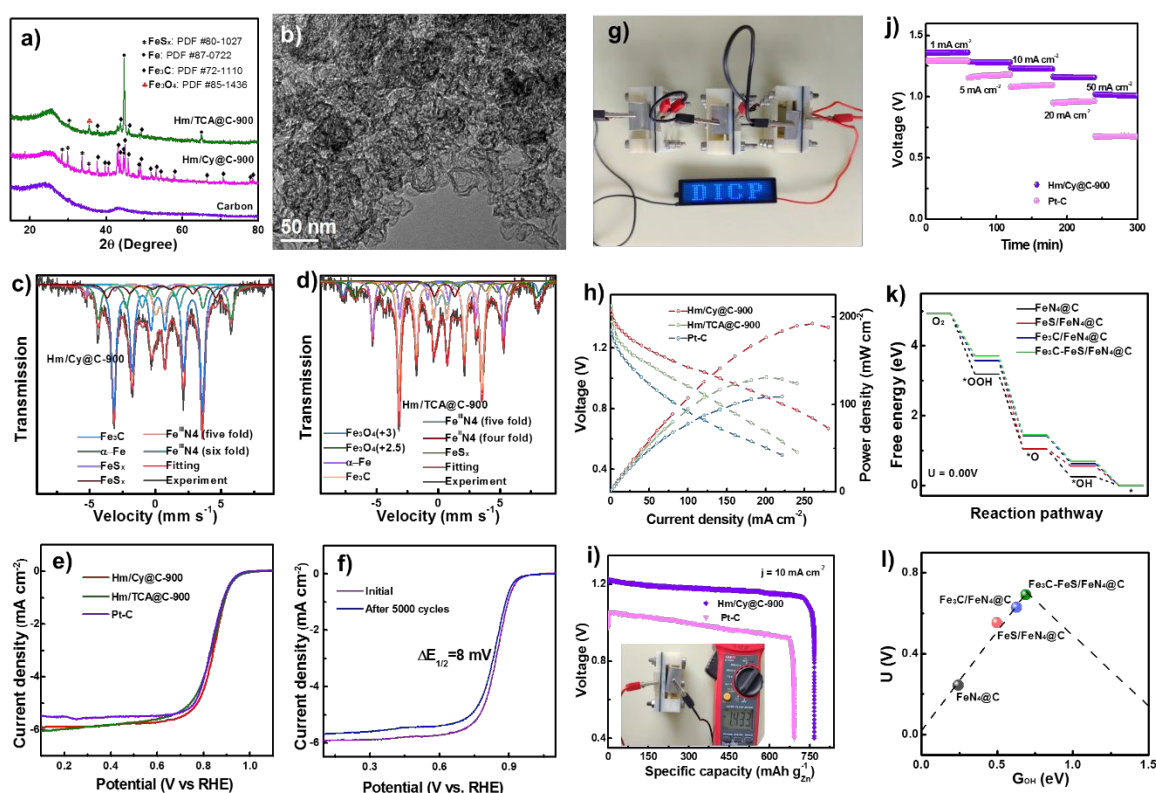


Figure 3 (a) XRD patterns. (b) High resolution TEM of Hm/Cy@C-900. Mössbauer spectra of (c) Hm/Cy@C-900 and (d) Hm/TCA@C-900. (e) LSV curves. (f) LSV curves of Hm/Cy@C-900 before and after 5000 cycles. (g) Image of ZAB turning on an LED. (h) ZAB polarization and power density. (i) Specific Hm/Cy@C-900 and Pt-C electrocatalyst discharging capabilities. (j) Battery discharge curves at various current densities. (k) U 0.00 V's ORR reaction pathway. (l) Free energy volcano diagram with ΔG_{OH} . Reproduced from ref.⁵⁷, Copyright 2023 Royal Society of Chemistry.



the cause of the different Fe contents in Hm/Cy@C-900 and Hm/TCA@C-900. The -COOH, -SH, and -NH₂ in N, S-containing ligands bind Fe atoms better than the =S and pyridinic N groups. Next, XRD was used to analyze the electrocatalyst compositions. Carbon ECP exhibited two wide diffraction peaks at ~20-30° and 40-45°, corresponding to graphitic carbon (002) and (101)⁷². In contrast, Hm/Cy@C-900 contains Fe₃C, FeS_x, and metallic Fe. Hm/TCA@C-900 has a novel Fe₃O₄ XRD pattern, Figure 3a, unlike Hm/Cy@C-900. Thus, Hm/TCA@C-900 should include Fe₃C, FeS_x, Fe₃O₄, and α -Fe nanoparticles. Unlike other iron salts, its metal macrocycle dissolvability permits iron-based species to self-assemble (Figure 3b). Solubility-induced scattering of Fe nanoparticles with carbon as active site accommodation was done by Shen et al.⁷³

Similarly, Hm/Cy@C-900 and Hm/TCA@C-900 composites have 0.39-0.40 at% S. Hm/Cy@C-900 (39.4%) has more C-S-C species than Hm/TCA@C-900 (32.6%), making it more conducive to carbon-S defects. C-S, C-N, and C=N imply that the N and S heteroatoms have been successfully co-doped into the carbon matrixes alongside Figure 3c's element mapping. The Fe 2p XPS spectrum is too faint to identify the Hm/TCA@C-900 electrocatalyst's iron species. So, we used ⁵⁷Fe Mössbauer spectra to study the iron components in these Fe-based electrocatalysts. It is shown in Figure 3f, the ORR electrocatalyst performance of Hm/Cy@C-T and Hm/TCA@C-900 electrocatalysts with 20 wt% Pt-C. Figure 3g also shows the Hm/Cy@C-900 electrocatalyst accelerated durability test. After 5000 cycles, the Hm/Cy@C-900 electrocatalyst showed just an 8 mV change in E_{1/2}, suggesting it may be durable enough for practical applications. A blue LED screen with DICP writing is illuminated by ZABs that have been built from Hm/Cy@C-900 and coupled in series, as shown in Figure 3h. In comparison to Hm/TCA@C-900 (131 mW

cm⁻²@201.2 mA cm⁻²) and 20 weight percent Pt-C (109 mW cm⁻²@221.3 mA cm⁻²), Figure 3i demonstrates that Hm/Cy@C-900 had a higher power density of 192 mW cm⁻² at 260.7 mA cm⁻². These parameters affect the power production and gas diffusion for incorporated electrocatalysts (10 mg cm⁻²) in Zn-air batteries, especially at elevated current densities. With an open-circuit voltage of 1.433 V (Figure 3j, inset) and a specific capacity of 766.0 mA h g⁻¹@10 mA cm⁻², the Hm/Cy@C-900 electrocatalysts were much more powerful than the Pt-C-assembled battery (691.5 mA h g⁻¹@10 mA cm⁻²). In contrast to the ZAB built by Pt-C, the Hm/Cy@C-900 battery displays a consistent discharge voltage at 50 mA cm⁻² (Figure 3k). Overall, the Hm/Cy@C-900 electrocatalyst performed best in ZAB studies. Computational simulations show that the reduction step of O* to OH* is the RDS for FeS/FeN₄@C in ORR, but it has a very strong O* chemisorption, leading to a great activation barrier. And the last step of OH* to OH⁻ is RDS for FeN₄@C, Fe₃C/FeN₄@C, and Fe₃C-FeS/FeN₄@C, which have a relatively weak O* chemisorption strength and facilitates the ORR process. Furthermore, the offset of d-band center of Fe₃C-FeS/FeN₄@C was much larger than these of FeN₄@C, Fe₃C/FeN₄@C and FeS/FeN₄@C systems, indicating that either FeS or Fe₃C clusters synergizes with single sites of FeN₄ to improve the ORR activity.

OER

The morphology of ANC-Fe_xNi_y is shown in Figure 4a by TEM. The HAADF-STEM picture shows ANC-Fe_xNi_y has an even size of around 1-2 nm, because to the high nucleation rate and low interfacial tension of ILs^{75, 76}. According to atomic force microscopy (AFM), ANC-Fe₁Ni₂ samples have a thickness of roughly 1.2–1.6 nm. (Figure 4b), indicating nanosphere shape due to surface ILs agent protection^{77, 78}. Tyndall effect is well seen in the ANC-Fe_xNi_y solution (Figure

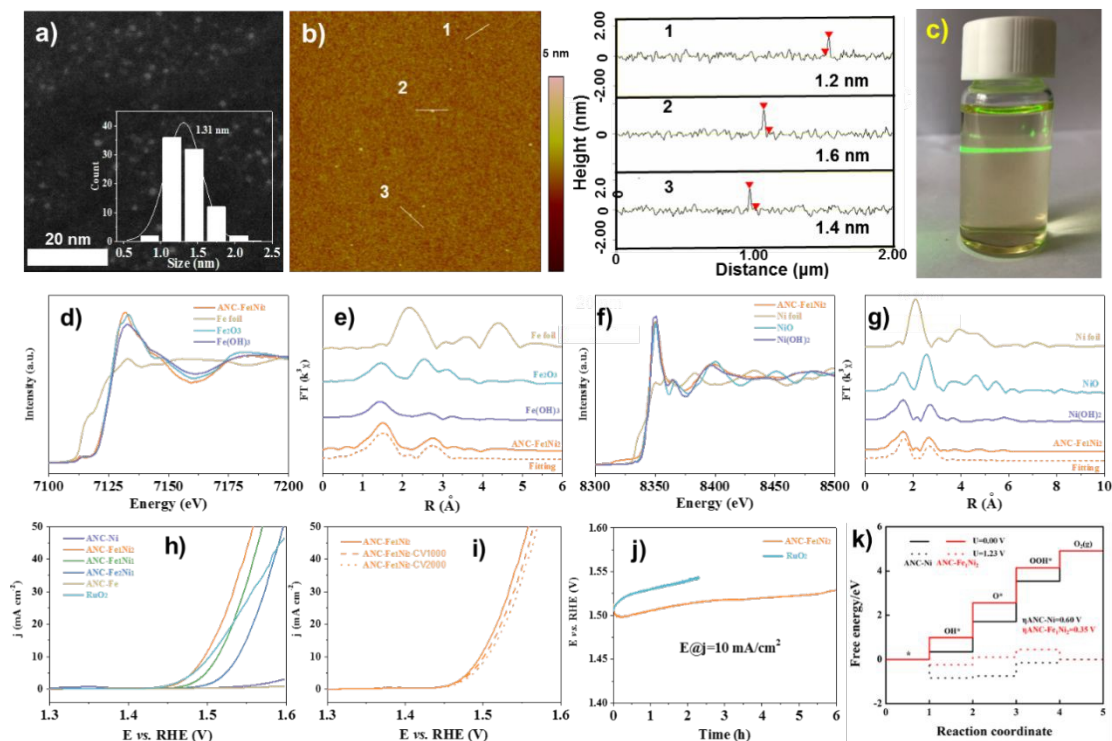


Figure 4 (a) HAADF-STEM, (b) AFM image with height profiles, and (c) Tyndall effect of ANC-Fe₁Ni₂ catalyst. (d) Fe K-edge XANES, (e) Fourier-transformed Fe K-edge, (f) Ni K-edge XANES, and (g) Fourier-transformed Ni K-edge of ANC-Fe₁Ni₂. (h) LSV curves (before and after 1000/2000 CV cycles) of ANC-Fe₁Ni₂. (i) Tafel plots. (j) Durability tests. (k) Calculated OER free energy diagram. Reproduced from ref.⁷⁴, copyright 2022 from Royal Society of Chemistry Royal.



4c), indicating outstanding dispersibility and subsequent OER electrode construction⁷⁹. The ANC-Fe_xNi_y catalysts' OER performance in 1 M KOH electrolyte was studied to maximize the Fe/Ni ratio. It is revealed in Figure 3h that the ANC-Fe₁Ni₂ cluster has the lowest overpotential (266 mV vs. RHE). LSV curves of ANC-Fe₁Ni₂ catalyst after 1000 and 2000 cycles are shown in Figure (i). The potential losses at 10 mA cm⁻² are 1 and 4 mV. These findings show that ANC-Fe₁Ni has good electrochemical activity and OER endurance.^{80, 81} The chronopotentiometry measurements (Figure 3f) reveal that ANC-Fe₁Ni is stable at 10 mA cm⁻² for 6 h. Also, ANC-Fe₁Ni catalyst LSV curves after 1000 and 2000 cycles. The potential losses at 10 mA cm⁻² are 1 mV and 4 mV. These findings show that ANC-Fe₁Ni has good electrochemical activity and OER endurance.

MnCoO_x with a cubic structure was determined by XRD (Figure 5a).^{82, 83} XRD patterns of MnCoO_x samples showed no reflections for MnO_x species because of the manganese ions' scattering inside the cobaltous matrix, even at high MnO_x concentrations (~40 mol%). XRD pattern of MnCoO_x catalysts with different doping levels showed a small shift towards lower angles around 36.8° for (311) as Mn dopants increased, suggesting that Mn cations were well doped into the Co₃O₄ lattice to produce solid solutions. We also examined Mn₁Co₅O_x annealed at various temperatures using XRD. At 200 °C, Co₃O₄ developed its crystalline phase. High-temperature calcination enhanced crystallinity. Despite annealing at 500 °C, Mn₁Co₅O_x composites showed no Mn oxide peaks, suggesting thermal stability. TEM was used to study MnCoO_x solid solutions for elemental composition and morphology. TEM scans showed most oxide

particles were 6–8 nm and expose Co₃O₄(220) and (311) planes (Figure 5b).^{84–86} Interestingly, the MnO_x species has no lattice fringes, suggesting that Mn was doped in Co₃O₄.

The linear-scanning profiles in Figure 5c showed that Mn atoms were scattered inside Co₃O₄'s lattice. The line sweep region has uniform lattice fringes and a distribution of components that shows Co and Mn coexist with Co being more abundant. The elemental mapping (Figure 5d) supports the homogeneity of Co and Mn species in MnCoO_x solid solutions. XANES spectra at Co and Mn K-edge were used to study Mn₁Co₅O_x's electrical structure and local coordination.⁶⁸ Mn₁Co₅O_x has a peak intensity equal to Co₃O₄ but distinct from Co-foil (Figure 5e). Also, Mn₁Co₅O_x's pre-line matches Co₃O₄. This indicates that Mn₁Co₅O_x's primary Co species valence states are Co²⁺ and Co³⁺. In contrast, the XANES spectra at Mn K-edge showed that Mn₁Co₅O_x has a substantially greater peak intensity of the white line than Mn₂O₃ and Mn₂O₃. Mn₁Co₅O_x's pre-line moved toward higher binding energies than Mn₂O₃, suggesting that its average Mn species valence should be greater than +3. It also shows potassium permanganate oxidation-related electron shortage around the Mn site. The Mn₁Co₅O_x catalyst's cooperation context was investigated using an R-space extended X-ray absorption fine structure (EXAFS) fitting analysis at the Co and Mn K-edges, as depicted in Figures 5g and 5h. The Co-O bond distance in Mn₁Co₅O_x increased from 1.81 Å to 1.83 Å against the control group of CoOOH. In contrast, Mn₁Co₅O_x reduced the Co-O bond distance from 1.91 Å to 1.83 Å compared to Co₃O₄.⁷⁴ Mn₁Co₅O_x reduced the Mn-O bonding distance from 1.80 Å to 1.67 Å compared to Mn₂O₃, likely owing to

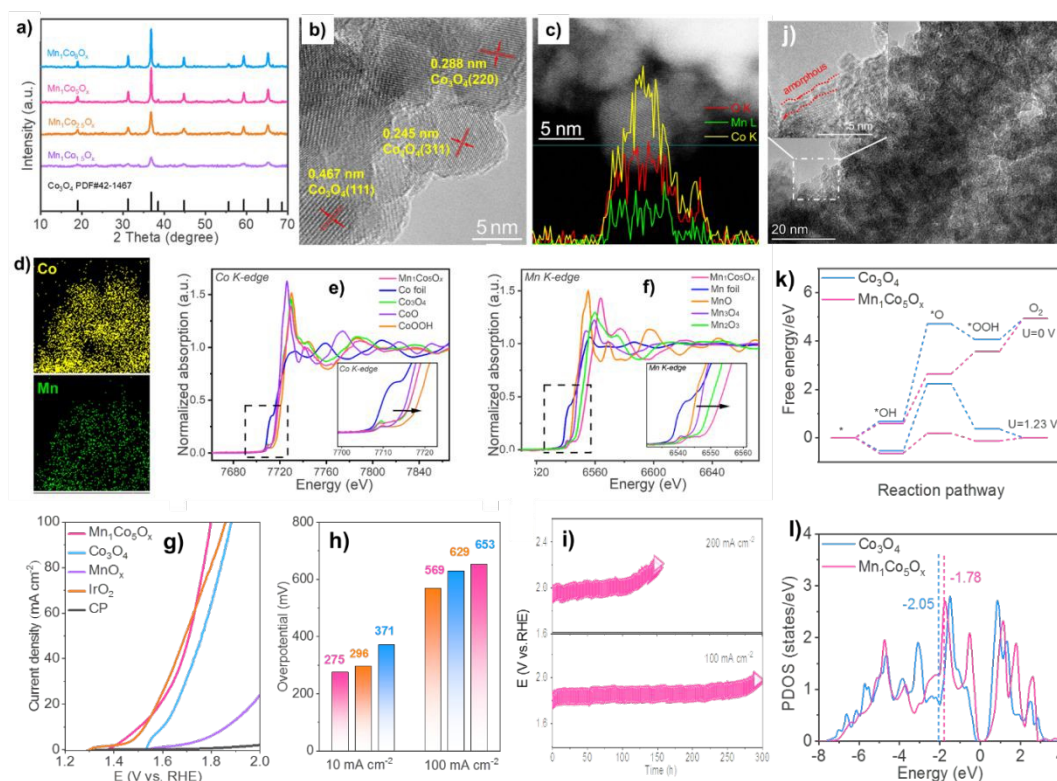


Figure 5 (a) XRD patterns. The catalyst's cross-section was profiled by linear scanning in (c). (b, d) HAADF-STEM picture with elemental mapping. XANES spectra of (e) Co and (f) Mn K-edge. (g) OER polarization curves and (h) overpotentials. (i) Chronopotentiometric measurements. (j) STEM picture of used Mn₁Co₅O_x. (k) OER routes' reaction-free energies at 0 and 1.23 volts. (l) Co activity sites' d-band center. Reproduced from ref. ⁵² copyright 2023 from Royal Society of Chemistry.



Mn's valence state being greater than +3. The electron density of $\text{Mn}_1\text{Co}_5\text{O}_x$'s Co-O bonds was comparable to Co_3O_4 , but somewhat greater than CoOOH and shorter. Compared to Mn_2O_3 , $\text{Mn}_1\text{Co}_5\text{O}_x$ has a lower electron density in its Mn-O bonds. This difference in electron density facilitated the creation of a solid-solution structure with a roughly uniform M-O bond length and expedited the flow of electrons between the Mn and Co atoms, hence enhancing OER catalytic activity.

The $\text{Mn}_1\text{Co}_5\text{O}_x$ composite outperformed Co_3O_4 , MnO_x , CP support, and IrO_2 in terms of catalytic efficiency, as indicated by the OER polarization curves (Figure 5i). This suggests that the OER took place on the surface. $\text{Mn}_1\text{Co}_5\text{O}_x$ specifically showed overpotentials of 275 and 569 mV at current densities of 10 and 100 mA cm^{-2} . (Figure 5j). $\text{Mn}_1\text{Co}_5\text{O}_x$'s increased catalytic OER performance is due to Mn-Co collaboration. The $\text{Mn}_1\text{Co}_5\text{O}_x$ catalyst had a ~15-fold increase in lifetime compared to Co_3O_4 at 100 mA cm^{-2} (Figure 5k), suggesting a 20.9% Mn dopant. The CP support is located at $2\theta = 26.5^\circ$. The $\text{Mn}_1\text{Co}_5\text{O}_x$ catalyst's TEM image exhibited an amorphous layer of ~1 nm thickness (Figure 5l), confirming $\text{Co}(\text{OH})_x$ production. XPS was also used to analyze the makeup of the pristine surface and its level of oxidation and used MnCoO_x catalysts. Conversely, the intermediate O^* has the maximum activation energy, which is thermodynamically unfavorable. After Mn doping,⁷¹ OER overpotential drops from 2.79 eV ($\text{Co}_3\text{O}_4(311)$) to 0.82 eV ($\text{MnCoO}_x(311)$). Figure 5n shows that Mn may raise Co_3O_4 's d-band center position from -2.05 eV to near the Fermi level (-1.78 eV). Interestingly, Ov equilibrates the active site's d-band center ($E_d = -1.88$ eV). Moderate intermediate species adsorption may reduce the OER reaction energy barrier. Thus, Mn and Ov stabilize reaction intermediates, lowering the OER reaction energy barrier and improving catalytic activity.⁷² Results of theoretical simulations match experimental phenomena.

We created the hybrid MnRuO_x catalyst using RuCl_3 and KMnO_4 as metal precursors and controlled crystallization at different annealing temperatures using a simple Pechini approach (Figure 6a). Operando X-ray diffraction (XRD) investigation tracked the catalyst crystal phase shift in response to temperature to determine how temperature affects crystallization, Figure 6b.⁸⁷ XRD spectra of MnRuO_x calcined at 300–350°C show an amorphous phase without visible precursor peaks. MnRuO_x -300 exhibits no distinguishing peaks due to its homogeneous crystal and amorphous dispersion. XRD patterns showed that MnRuO_x hybrid material crystallizes virtually entirely at temperatures over 400 °C, containing Ru oxides. The MnRuO_x particle is ~4–5 nm in size (Figure 6c) and exposes $\text{RuO}_2(110)$ and (101) planes.⁸⁹ An amorphous phase filled the interstitial spaces between the microcrystalline phases, according to the STEM image. The 3D atomic overlap Gaussian fitting findings from the high-angle annular dark-field scanning transmission electron microscopy (HAADF-STEM) pictures showed diverse atomic configurations in different locations.⁹⁰ Region 1 had irregular atoms, indicating an amorphous structure (Figure 6d and 6e). Region 2 had consistent atom arrangements, suggesting microcrystalline structures (Figure 6f and 6g). These findings support the MnRuO_x -300 catalyst heterostructures. Thus, the MnRuO_x catalyst has both microcrystalline and amorphous structures, with RuO_2 crystals in the microcrystalline part. Linear scanning analysis of individual particles revealed a homogenous distribution of Mn and Ru elements, generating a doped

phase in the limited size range (Figure 6h).⁶⁸ Local nanoscale elemental line scan investigation shows homogeneous Mn and Ru distribution in solid solution. A large-scale elemental mapping study verifies Mn and Ru's uniform distribution in the catalyst sample.⁵⁶

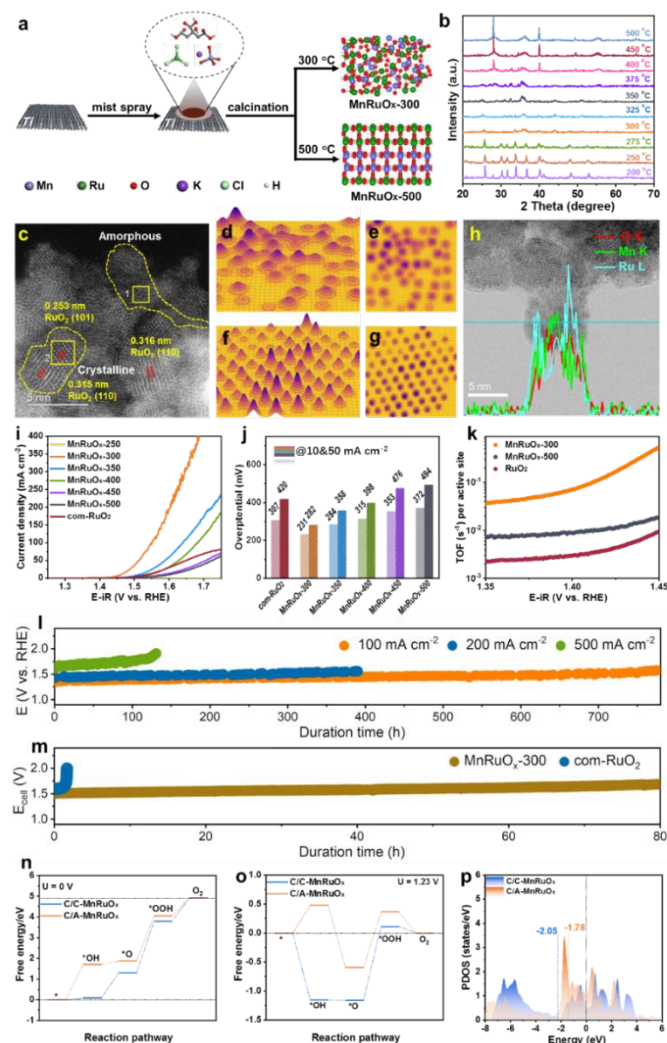


Figure 6 (a) Schematic preparation of the MnRuO_x catalyst. (b) Operando XRD of MnRuO_x -150 precursor treated at different temperatures. (c) HAADF-STEM image of MnRuO_x -300 showcases the coexistence of microcrystalline and amorphous phases. 3D atomic overlap Gaussian fitting on selected STEM region 1 (d, e) and region 2 (f, g). (h) HR-TEM and line scan elemental mapping. (i) Polarization curves, (j) Overpotential bar charts, and comparison of turnover frequency (TOF). (l) Durability tests of MnRuO_x -300@TF in an H-type electrolysis cell. (m) Chronopotentiometry testing at 100 mA cm^{-2} in the PEMWE electrolyser at 80°C. The energy profile of OER at (n) $U = 0$ V and (o) $U = 1.23$ V. (p) Projected DOS. Reproduced with permission from ref. ⁸⁸, copyright 2024 from Wiley VCH.

MnRuO_x samples were tested for linear sweep voltammetry (LSV) under acidic circumstances and compared to com-RuO_2 (Figure 6i). The best OER catalyst was MnRuO_x -300. At 10 mA cm^{-2} , RuO_2 had an overpotential of 307 mV, consistent with prior results.^{91, 92} However, a bar chart of the samples' overpotentials at various temperatures showed a significant rise with higher annealing temperatures (Figure 6j). The MnRuO_x -300 catalyst, with its amorphous homogenous structure and microcrystalline particles, had the lowest overpotential (231 mV at 10 mA cm^{-2} and 282 mV at 50



mA cm⁻²). Additional Tafel slopes were generated to assess catalyst OER kinetics. Comparison of turnover frequencies (TOF) at 1.44 V shows considerable differences between RuO₂, MnRuO_x-500, and MnRuO_x-300 catalysts (Figure 6k). The TOF of MnRuO_x-300 is 0.071 s⁻¹, substantially higher than MnRuO_x-500 (0.0088 s⁻¹) and RuO₂ (0.0030 s⁻¹). The catalyst treated at 300 °C has amorphous and crystalline structures, hence it has better OER activity. Stability experiments were performed on MnRuO_x-300@TFF samples in acidic circumstances (pH=0) at varying current densities using an H-type electrolysis cell. Durability studies of ~780 hours at 100 mA cm⁻², ~400 h at 200 mA cm⁻², ~130 h at 500 mA cm⁻², and ~30 h at 1.0 A cm⁻² (Figure 6l) indicate good catalyst stability at high current densities. Under 100 mA cm⁻² for 80 h, the MnRuO_x-300 cell maintained PEMWE performance, but a RuO₂ anode only lasts around 1 hour (Figure 6m). All reaction steps are endothermic at U = 0 V. At the *O formation to *OOH stage, C/C-MnRuO_x and C/A-MnRuO_x heterostructures have OER RDS. The OER overpotentials of C/A-MnRuO_x and C/C-MnRuO_x are 1.28 eV and 0.96 eV, respectively, at U = 1.23 V, proving that it decreases it. We estimated the predicted density of states (DOS) for C/C-MnRuO_x and C/A-MnRuO_x heterostructures (Figure 6p). The d-band center model describes adsorbate-metal interactions well.⁹³ After amorphization, the DOS at the Fermi level rises, raising the d-band center energy level.

Electrosynthesis of Urea with Nitrate and Carbon Dioxide

Simple pyrolysis of Fe^{III}: PVP compounds with carbon ECP at 700 °C in Ar produced the FeNC-Fe₁N₄/C nanocomposite. Figure 7a shows FeNC-Fe₁N₄ exhibits metallic Fe particles and the carbon support has high defect and disordered carbon matrix population, promoting electroconductibility and activity during electrocatalysis⁹⁴. It verified that FeNC-Fe₁N₄/C contained mostly Fe species and carbon matrix. STEM using EDX elemental mapping technology also examined the distribution of atomically distributed Fe single atoms and metallic Fe clusters. High-resolution TEM images (Figure 7b) showed metallic Fe(200) facet, and size of Fe clusters is ~ 4-7 nm.

A typical three-electrode setup in an H-type cell under continuous CO₂ flow with Nafion 117 membranes between the cathode and anode chambers was used to assess urea electrosynthesis performance. Figure 7d ranks FeNC-Fe₁N₄/C current densities: KNO₃ > KHCO₃+CO₂ > KHCO₃+KNO₃ > KHCO₃+CO₂. Research indicates that the co-electrolysis of CO₂ and NO₃⁻ for urea production has a lower current density than CO₂RR and NO₃RR. Results show that CO₂RR, NO₃RR, and competing HER are effectively regulated, ensuring high urea FE in co-reduction.⁹⁶ Figure 7e displays FeNC-Fe₁N₄/C sample urea yield rates: 2.1, 3.9, 8.7, 26.9, 30.3, 36.5, 38.2, and 24.6 mmol g_{cat}⁻¹ h⁻¹ at -0.3, -0.4, -0.5, -0.6, -0.7, -0.8, -0.9, and -1.0 V, respectively. Urea FEs rise and fall when the applied potential is lowered to -1.0 V. Optimal urea production is 38.2 mmol g_{cat}⁻¹ h⁻¹ at -0.9 V, and urea FE of 66.5% at -0.6 V surpasses existing electrocatalysts. Figure 7f shows that urea dominates at 60% between -0.3 and -0.6 V, followed by NH₃ and H₂ FEs at 20% and 10%, respectively. When the potential is changed downward, FEs of competing NH₃, H₂, and NO₂⁻ rise, corresponding to a rapid increase in current density about -0.6 V in LSV curves.

To understand the complex C- and N-species in co-electrolysis, it is crucial to identify the reaction route and capture important

intermediates in C-N coupling.⁹⁷ It is depicted in (Figure 7g,h) FeNC-Fe₁N₄/C time-resolved *in-situ* Raman spectra at -0.6 V during urea electrosynthesis. Vibration peaks at 589, 1401, 1568, and 1682 cm⁻¹ correspond to OCN bending, adsorbed C-H in-plane bending, δ_{NH2}, and C=O stretch modes in formamide. However, ¹H-NMR spectroscopy shows urea production in electrolyte, not formamide. We infer that *CONH₂ is the intermediary in C-N coupling for urea production. As CO is the reduction product in CO₂RR, nucleophilic attack of *CO and *NH₂ was used to create C-N coupling. Raman spectra showed a modest signal of *CO at 2080 cm⁻¹, supporting this finding (Figure h). The C-N stretch mode of urea at 1000 cm⁻¹ is not seen in Raman spectra owing to its feeble vibration signal⁹⁸. The free energy diagrams in Figure 7i depict the chemical pathways of NO₃⁻ reduction to *NH₂ on Fe₁₃-Fe₁N₄/C.

The RDS for Fe₁₃-Fe₁N₄/C and Fe₁N₄/C is *NO₃ to *NO₃H and *NO to *NOH, respectively, and the energy barrier of RDS on Fe₁₃-Fe₁N₄/C is comparative lower than that on Fe₁N₄/C, suggesting that nitrate reduction is more favorable on Fe₁₃-Fe₁N₄/C. Next, there are more electron transfer between *NO₃, *NO₃H and *COOH intermediates and Fe₁₃-Fe₁N₄/C. While, the adsorption of *COOH intermediate is compromised and spatial constraints due to steric hindrance, as it resides at the interface of Fe cluster and Fe₁N₄ site. In all, the Fe cluster and Fe₁N₄ in Fe₁₃-Fe₁N₄/C are the primary active site for nitrate reduction and CO₂ reduction and C-N coupling, respectively.

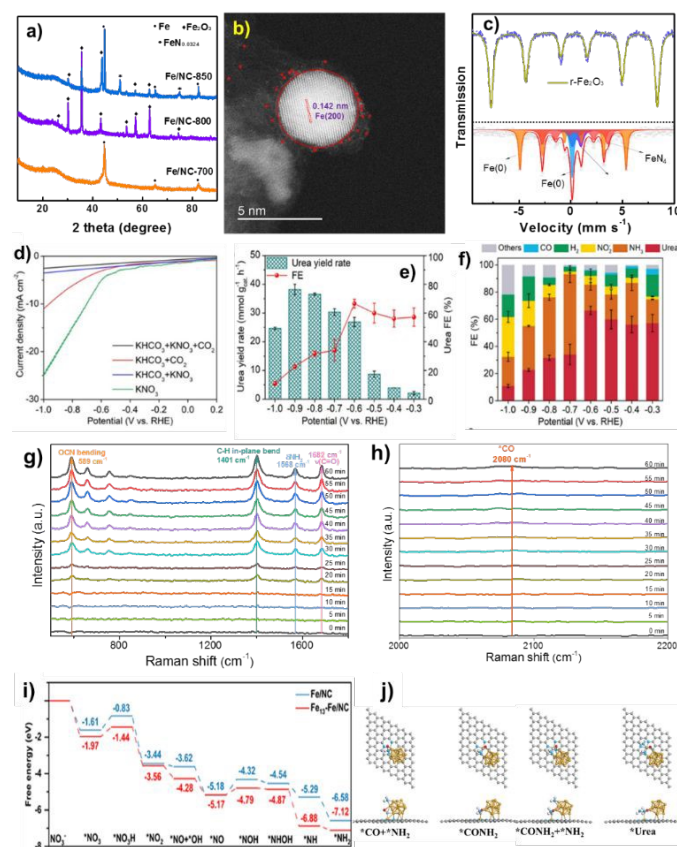


Figure 7 (a) XRD, (b) STEM image, (c) Mössbauer spectra, (d) LSV curves, (e) potential-dependent urea yield rate, and (f) FEs (at -0.6 V) of FeNC-Fe₁N₄/C. (g,h) Time-resolved *in-situ* Raman spectra in urea electrosynthesis at -0.6 V. (i) Free energy diagrams of NO₃⁻ reduction to *NH₂. (j) Structure diagrams of the C-N coupling process on Fe₁₃-Fe₁N₄/C. Reproduced from Ref. ⁹¹, copyright 2024 from Wiley WCH.



Conclusions and Future progression

Research on water oxidation and electrocatalysis shows a variety of ways to increase catalytic stability and activity. They show the synergistic effect of cobalt clusters-CoN_x composites for electrochemical oxygen reduction, Investigating the promotion effect of active sites in iron-based oxygen reduction electrocatalysts for Zn-air batteries., and the high activity for sustainable acidic water oxidation through intrinsically robust cubic MnCoO_x solid solutions. They also discuss heterogeneous catalysis promoted by ultrafine amorphous metallic hydroxide nanoparticles and oxygen vacancy-rich amorphous FeNi nanoclusters modified by ionic liquids. These findings help develop stable and effective electrocatalysts for energy storage and conversion.

Overall, the highlighted study shows how atomically exact metal nanoclusters and metal oxide clusters may revolutionize electrocatalysis. Researching Fe-based oxygen reduction electrocatalysts have the potential to greatly enhance the performance of zinc-air batteries. This Li et al. discovery emphasizes the need for several active sites for catalytic effectiveness. Zhang et al. showed that cubic MnCoO_x solid solutions are durable and efficient, demonstrating metal oxide clusters' potential for persistent water oxidation and scalable hydrogen production. Zhang et al.'s Investigation of the synergistic effect of cobalt clusters-CoN_x composites on electrochemical oxygen reduction highlights the potential for developing customized catalysts. These examples demonstrate the need to properly manage catalyst shape and composition to increase catalytic activity and lifespan. In addition, catalyst design and production have been successful, but commercializing and scaling up these advanced electrocatalysts has proven difficult. According to Cao et al., optimizing synthesis processes and studying cheap precursor materials would enable large-scale catalytic material fabrication and deployment. The research found that improving integration and electrochemical systems maximize energy conversion efficiency, lifespan, and cost. These studies demonstrate the revolutionary potential of atomically precise metal nanoclusters and metal oxide clusters in electrocatalysis for sustainable energy technologies, which could lead to cleaner, greener energy sources. Future development may need further electrocatalyst design and manufacturing optimization to increase activity, stability, and selectivity for electrochemical reactions such as oxygen reduction, water oxidation, and energy conversion.

Essential areas of attention might be:

1. Nanostructuring and Active Site Engineering: Researchers are customizing active sites and improving catalytic activity using nanomaterials and atomically precise metal nanoclusters. Identifying catalytic active sites has fascinated academics for decades and is crucial. Active sites may be single atoms or groups of atoms on metal particles. Future research should focus on developing innovative techniques to accurately observe the intricate steps of catalytic reactions at the catalytic site, achieving spatiotemporal accuracy in milliseconds. This endeavor presents a challenging yet highly promising opportunity. Understanding the electronic structure of TMO oxides via theoretical studies can help explain catalytic processes. In heterogeneous catalysis, learning the existence and structure of active sites is a huge difficulty, but combining experiments and theory should help. High stability of TMO clusters

and novel methods for very stable catalysts throughout catalytic processes may aid mechanistic studies. DOI: 10.1039/D4CC02722A

2. Synergism in Multifunctional Materials: Composite materials and multifunctional catalysts are being studied to boost catalytic activity and durability. Examining the oxidation state, atom dispersion, and potential behavior of heteroelements is crucial when examining the catalytic properties of the doped element in an alloy catalyst. This information is hard to get. Thus, future research should combine experimentation and theory and build new tools. The link between multifunctional TMO nanomaterials' geometric and electrical characteristics and catalytic reactivity remains a priority. The fundamental ideas of bimetallic and multimetallic nanocatalysis synergy will influence the composition choices of high-performance nanocatalysts for specific chemical reactions.

3. Understanding Reactions Using In-Situ and Operando Characterization: A deeper understanding of molecular-level reaction mechanisms might influence selectivity and efficiency-enhancing electrocatalyst design.^{99,100} It is important to have a way to analyze TMO catalysts in real time and real space to obtain a more profound comprehension of the catalytic reaction process, its kinetics, as well as the occurrence of coking and leaching. Studying the high fluxionality of a few TM atom clusters at elevated temperatures and determining whether the nanocluster structure undergoes reversible or irreversible dynamic changes can be achieved through in-situ and operando extended X-ray absorption fine structure (EXAFS) and diffuse reflectance infrared Fourier-transform spectroscopy (DRIFT). Future research should focus on developing advanced in-situ and operando technologies, such as high-resolution imaging and spectroscopy, to better understand and address these challenges. An analysis of this nature would be instrumental in exploring the catalytic factors of TM clusters.

4. Studying new high-entropy oxide clusters: Investigation of metal-organic frameworks and ionic liquids as electrolytes and electrocatalysts for devices that convert and store energy. When combined with metal-organic frameworks (MOFs) and ionic liquids (ILs), high-entropy oxide (HEO) clusters—which are defined by several metal cations dispersed randomly inside a single-phase lattice—offer promising advances in energy conversion and storage technologies. Because of their large surface area and adjustable porosity, metal oxide frameworks (MOFs) are a great approach to enhance heteroelectrolytes' ion mobility and structural integrity. Additionally, the metal nodes inside MOFs can function as active catalytic sites. In addition to these hybrids, ILs enhance the electrode-electrolyte interactions by offering a favorable ionic environment due to their high ionic conductivity and stability. The cooperation of HEOs, MOFs, and ILs may be used to create novel materials with enhanced catalytic performance and customized characteristics, greatly enhancing the longevity and efficiency of fuel cells, batteries, supercapacitors, and electrolyzers.

5. Single-Atom and Single-Electron Tailoring: Atomically precise nanochemistry may govern TMO clusters in new ways, opening up fascinating catalytic research options. Quantum-sized clusters' electronic characteristics are subject to atom count. Customized nanocluster catalysts allow atom-by-atom catalytic reactivity tailoring. Accurate nanocatalysts would not be able to produce novel catalytic phenomena like spin effects in chemical processes, but precise regulation of nanocluster attraction at the single-electron level would.



6. Scale-up and Commercialization: This involves improving manufacturing methods and adding advanced electrocatalysts to useful products for affordability, scalability, and sustainability.

The area is well-positioned for sustained innovation and interdisciplinary cooperation to tackle global energy concerns and propel the shift towards a more sustainable energy future.

Author contributions

The manuscript was collaboratively written by all authors. The final version of the manuscript has been approved by all authors.

Conflicts of interest

There are no conflicts to declare.

Acknowledgements

We acknowledge the financial support by National Natural Science Foundation of China (22172167).

Notes and references

- H. Dong, M. Xue, Y. Xiao and Y. Liu, *Sci. Total Environ.*, 2021, **758**, 143688.
- F. K. Busari, Z. Babar, A. Raza and G. Li, *Sust. Mater. Technol.*, 2024, **40**, e00958.
- H. Bai, D. Chen, Q. Ma, R. Qin, H. Xu, Y. Zhao, J. Chen and S. Mu, *Electrochem. Energy Rev.*, 2022, **5**, 24.
- J. Z. Hassan, A. Zaheer, A. Raza and G. Li, *Sust. Mater. Technol.*, 2023, **36**, e00609.
- T. Guo, L. Li and Z. Wang, *Adv. Energy Mater.*, 2022, **12**, 2200827.
- L. Liu and A. Corma, *Chem. Rev.*, 2018, **118**, 4981-5079.
- Y. Song, C. Zhou and R. Jin, in *Crystallization via Nonclassical Pathways Volume 1: Nucleation, Assembly, Observation & Application*, ACS Publications, 2020, pp. 47-71.
- F. Li, G.-F. Han and J.-B. Baek, *Acc. Mater. Res.*, 2021, **2**, 147-158.
- J. Gao, H. Tao and B. Liu, *Adv. Mater.*, 2021, **33**, 2003786.
- R. Jin, G. Li, S. Sharma, Y. Li and X. Du, *Chem. Rev.*, 2020, **121**, 567-648.
- Z. Yang, J. Zhang, M. C. Kintner-Meyer, X. Lu, D. Choi, J. P. Lemmon and J. Liu, *Chem. Rev.*, 2011, **111**, 3577-3613.
- Y. Zhang, Z. Li, J. Zhang, L. Xu, Z. Han, A. Baiker and G. Li, *Nano Res.*, 2023, **16**, 8919.
- S. Lu, J. Liang, H. Long, H. Li, X. Zhou, Z. He, Y. Chen, H. Sun, Z. Fan and H. Zhang, *Acc. Chem. Res.*, 2020, **53**, 2106-2118.
- Y. Guo, S. Mei, K. Yuan, D.-J. Wang, H.-C. Liu, C.-H. Yan and Y.-W. Zhang, *ACS Catal.*, 2018, **8**, 6203-6215.
- Z. Li, L. Xu, Z. Babar, A. Raza, Y. Zhang, X. Gu, Y. Miao, Z. Zhao and G. Li, *Nano Res.*, 2024, **17**, 4729.
- Y. Du, H. Sheng, D. Astruc and M. Zhu, *Chem. Rev.*, 2019, **120**, 526-622.
- Q. Shi, Y. Zhang, Z. Li, Z. Han, L. Xu, A. Baiker and G. Li, *Nano Res.*, 2023, **16**, 6951.
- S. Barkaoui, Y. Wang, Y. Zhang, X. Gu, Z. Li, B. Wang, G. Li and Z. Zhao, *ISCIENCE*, 2024, 110255.
- Z. Li, J. Zhang and G. Li, *Chin. J. Struct. Chem.*, 2024, **43**, 100300.
- Z. Qin, Z. Li, S. Sharma, Y. Peng, R. Jin and G. Li, *Research*, 2022, 0018. DOI: 10.1039/D4CC02722A
- Y. Sun, Q. Shi, X. Gu, B. Wang, B. Lumbers and G. Li, *J. Coll. Interface Sci.*, 2024, **662**, 76.
- Q. Shi, X. Zhang, Z. Li, A. Raza and G. Li, *ACS Appl. Mater. Interfaces*, 2023, **15**, 30161.
- K. Kwak and D. Lee, *Acc. Chem. Res.*, 2018, **52**, 12-22.
- P. Sanwal, A. Raza, Y.-X. Miao, B. Lumbers and G. Li, *Polyoxometalates*, 2024, **3**, 9140057.
- C. Yao, N. Guo, S. Xi, C.-Q. Xu, W. Liu, X. Zhao, J. Li, H. Fang, J. Su and Z. Chen, *Nature Commun.*, 2020, **11**, 4389.
- Y. Chen, X. Gu, S. Guo, J. Zhang, S. Barkaoui, L. Xu and G. Li, *ChemSusChem*, 2024, **17**, e202400309.
- X. F. Lu, S. L. Zhang, E. Shangguan, P. Zhang, S. Gao and X. W. Lou, *Adv. Sci.*, 2020, **7**, 2001178.
- D. Friebel, M. W. Louie, M. Bajdich, K. E. Sanwald, Y. Cai, A. M. Wise, M.-J. Cheng, D. Sokaras, T.-C. Weng and R. Alonso-Mori, *J. Am. Chem. Soc.*, 2015, **137**, 1305-1313.
- Y. Yan, T. He, B. Zhao, K. Qi, H. Liu and B. Y. Xia, *J. Mater. Chem. A*, 2018, **6**, 15905-15926.
- M. Ledendecker, S. Krick Calderón, C. Papp, H. P. Steinrück, M. Antonietti and M. Shalom, *Angew. Chem. Inter. Ed.*, 2015, **54**, 12361-12365.
- J. Zhao, X. Li, M. Zhang, Z. Xu, X. Qin, Y. Liu, L. Han and G. Li, *Nanoscale*, 2023, **15**, 4612.
- J. Wang, J. Chen, P. Wang, J. Hou, C. Wang and Y. Ao, *Appl. Catal. B*, 2018, **239**, 578-585.
- H. Q. Fu, L. Zhang, C. W. Wang, L. R. Zheng, P. F. Liu and H. G. Yang, *ACS Energy Lett.*, 2018, **3**, 2021-2029.
- Y. Liu, Q. Li, R. Si, G. D. Li, W. Li, D. P. Liu, D. Wang, L. Sun, Y. Zhang and X. Zou, *Adv. Mater.*, 2017, **29**, 1606200.
- Y. Lin, G. Chen, H. Wan, F. Chen, X. Liu and R. Ma, *Small*, 2019, **15**, 1900348.
- P. Chen, T. Zhou, L. Xing, K. Xu, Y. Tong, H. Xie, L. Zhang, W. Yan, W. Chu and C. Wu, *Angew. Chem.*, 2017, **129**, 625-629.
- R. D. Smith, M. S. Prévot, R. D. Fagan, S. Trudel and C. P. Berlinguette, *J. Am. Chem. Soc.*, 2013, **135**, 11580-11586.
- Y. Huang, R. Yang, G. Anandhababu, J. Xie, J. Lv, X. Zhao, X. Wang, M. Wu, Q. Li and Y. Wang, *ACS Energy Lett.*, 2018, **3**, 1854-1860.
- C. Liang, P. Zou, A. Nairan, Y. Zhang, J. Liu, K. Liu, S. Hu, F. Kang, H. J. Fan and C. Yang, *Energy Environ. Sci.*, 2020, **13**, 86-95.
- J. Nai, H. Yin, T. You, L. Zheng, J. Zhang, P. Wang, Z. Jin, Y. Tian, J. Liu and Z. Tang, *Adv. Energy Mater.*, 2015, **5**.
- A. Dutta, A. K. Samantara, S. K. Dutta, B. K. Jena and N. Pradhan, *ACS Energy Lett.*, 2016, **1**, 169-174.
- Y. Xie, H. Li, C. Tang, S. Li, J. Li, Y. Lv, X. Wei and Y. Song, *J. Mater. Chem. A*, 2014, **2**, 1631-1635.
- W. Wang, Q. Jia, S. Mukerjee and S. Chen, *ACS Catal.*, 2019, **9**, 10126-10141.
- C. Xu, C. Guo, J. Liu, B. Hu, J. Dai, M. Wang, R. Jin, Z. Luo, H. Li and C. Chen, *Energy Storage Mater.*, 2022, **51**, 149-158.
- H. Xu, D. Wang, P. Yang, A. Liu, R. Li, L. Xiao, J. Zhang, Z. Qu and M. An, *Sust. Energy Fuels*, 2021, **5**, 2695-2703.
- Y. Lee, J. H. Ahn, H. Jang, J. Lee, S. Yoon, D.-G. Lee, M. G. Kim, J. H. Lee and H.-K. Song, *J. Mater. Chem. A*, 2022, **10**, 24041-24050.
- M. Lefèvre, E. Proietti, F. Jaouen and J.-P. Dodelet, *Science*, 2009, **324**, 71-74.
- Y. He, S. Liu, C. Priest, Q. Shi and G. Wu, *Chem. Soc. Rev.*, 2020, **49**, 3484-3524.
- S. N. Zhao, J. K. Li, R. Wang, J. Cai and S. Q. Zang, *Adv. Mater.*, 2022, **34**, 2107291.
- Y. Wang, Y. Zhang, Q. Jiang, S. Guo, A. Baiker and G. Li, *ChemCatChem*, 2022, **14**, e202200203.



- 51 Y. Wang, Q. Jiang, L. Xu, Z.-K. Han, S. Guo, G. Li and A. Baiker, *ACS Appl. Mater. Interfaces*, 2021, **13**, 61078-61087.
- 52 J. Zhang, A. Raza, Y. Zhao, S. Guo, Z. U. D. Babar, L. Xu, C. Cao and G. Li, *J. Mater. Chem. A*, 2023, **11**, 25345-25355.
- 53 J. Zhang, Y. Xie, Q. Jiang, S. Guo, J. Huang, L. Xu, Y. Wang and G. Li, *J. Mater. Chem. A*, 2022, **10**, 16920-16927.
- 54 X. Wu, H. Zhang, S. Zuo, J. Dong, Y. Li, J. Zhang and Y. Han, *Nano-micro letters*, 2021, **13**, 136.
- 55 J. Hu, W. Liu, C. Xin, J. Guo, X. Cheng, J. Wei, C. Hao, G. Zhang and Y. Shi, *J. Mater. Chem. A*, 2021, **9**, 24803-24829.
- 56 Y. Cao, S. Guo, C. Yu, J. Zhang, X. Pan and G. Li, *J. Mater. Chem. A*, 2020, **8**, 15767-15773.
- 57 Z. Li, Y. Xie, J. Gao, X. Zhang, J. Zhang, Y. Liu and G. Li, *J. Mater. Chem. A*, 2023, **11**, 26573-26579.
- 58 C. Dominguez, F. J. Perez-Alonso, M. A. Salam, J. L. Gomez de la Fuente, S. A. Al-Thabaiti, S. N. Basahel, M. A. Pena, J. L. G. Fierro and S. Rojas, *Int. J. Hydrog. Energy*, 2014, **39**, 5309-5318.
- 59 Z. Wang, C. Zhu, H. Tan, J. Liu, L. Xu, Y. Zhang, Y. Liu, X. Zou, Z. Liu and X. Lu, *Adv. Funct. Mater.*, 2021, **31**, 2104735.
- 60 L. Zhuang, Z. Jia, Y. Wang, X. Zhang, S. Wang, J. Song, L. Tian and T. Qi, *Chem. Eng. J.*, 2022, **438**, 135585.
- 61 W. Zhou, H. Su, Z. Wang, F. Yu, W. Wang, X. Chen and Q. Liu, *J. Mater. Chem. A*, 2021, **9**, 1127-1133.
- 62 X. Yang, Y. Wang, X. Wang, B. Mei, E. Luo, Y. Li, Q. Meng, Z. Jin, Z. Jiang, C. Liu, J. Ge and W. Xing, *Angew. Chem. Int. Ed.*, 2021, **60**, 26177-26183.
- 63 H. Yao, X. Wang, K. Li, C. Li, C. Zhang, J. Zhou, Z. Cao, H. Wang, M. Gu, M. Huang and H. Jiang, *Appl. Catal. B*, 2022, **312**, 121378.
- 64 X. Jiang, J. Chen, F. Lyu, C. Cheng, Q. Zhong, X. Wang, A. Mahsud, L. Zhang and Q. Zhang, *J. Energy. Chem.*, 2021, **59**, 482-491.
- 65 Z. Cui and X. Bai, *ACS Appl. Mater. Interfaces*, 2022, **14**, 9024-9035.
- 66 X. Ao, Y. Ding, G. Nam, L. Soule, P. Jing, B. Zhao, J. Hwang, J. Jang, C. Wang and M. Liu, *Small*, 2022, **18**, 2203326.
- 67 X. Xu, X. Zhang, Z. Xia, R. Sun, H. Li, J. Wang, S. Yu, S. Wang and G. Sun, *J. Energy. Chem.*, 2021, **54**, 579-586.
- 68 J. Zhang, Y. Xie, Q. Jiang, S. Guo, J. Huang, L. Xu, Y. Wang and G. Li, *J. Mater. Chem. A*, 2022, **10**, 16920-16927.
- 69 Z. Liang, H. Song and S. Liao, *J. Phys. Chem. C*, 2011, **115**, 2604-2610.
- 70 L. Li, S. Shen, G. Wei and J. Zhang, *Acta Phys. -Chim. Sin.*, 2021, **37**, 1911011.
- 71 C. Shu, Q. Tan, C. Deng, W. Du, Z. Gan, Y. Liu, C. Fan, H. Jin, W. Tang, X. d. Yang, X. Yang and Y. Wu, *Carbon Energy*, 2021, **4**, 1-11.
- 72 A. Raza, A. A. Rafi, J. Z. Hassan, A. Rafiq and G. Li, *Appl. Surf. Sci. Adv.*, 2023, **15**, 100402.
- 73 S. Shen, Z. Zhai, J. Qin, X. Zhang and Y. Song, *J. Porphyr. Phthalocya.*, 2019, **23**, 1013-1019.
- 74 Y. Cao, Y. Su, L. Xu, X. Yang, Z. Han, R. Cao and G. Li, *J. Energy Chem.*, 2022, **71**, 167-173.
- 75 H. Abroshan, G. Li, J. Lin, H. J. Kim and R. Jin, *J. Catal.*, 2016, **337**, 72.
- 76 J. Sun, N. Guo, Z. Shao, K. Huang, Y. Li, F. He and Q. Wang, *Adv. Energy Mater.*, 2018, **8**, 1800980.
- 77 M. Antonietti, D. Kuang, B. Smarsly and Y. Zhou, *Angew. Chem. Inter. Ed.*, 2004, **43**, 4988-4992.
- 78 H. Park, Y. S. Choi, Y. Kim, W. H. Hong and H. Song, *Adv. Funct. Mater.*, 2007, **17**, 2411-2418.
- 79 G. Kresse and J. Furthmüller, 1996.
- 80 D. Yan, Y. Li, J. Huo, R. Chen, L. Dai and S. Wang, *Adv. Mater.*, 2017, **29**, 1606459.
- 81 F. Sun, C. Li, B. Li and Y. Lin, *J. Mater. Chem. A*, 2017, **5**, 23103-23114.
- 82 T. Cai, H. Huang, W. Deng, Q. Dai, W. Liu and X. Wang, *Appl. Catal. B*, 2015, **166-167**, 393-405. DOI: 10.1039/D4CC02722A
- 83 J. Li, X. Liang, S. Xu and J. Hao, *Appl. Catal. B*, 2009, **90**, 307-312.
- 84 Q. Shi, Z. Li, C. Cao, G. Li, S. Barkaoui, *Nanoscale Adv.*, 2023, **5**, 5385.
- 85 Y. Sun, Q. Wang and Z. Liu, *ACS Appl. Mater. Interfaces*, 2022, **14**, 43508-43516.
- 86 S. Barkaoui, Z. Li, C. Cao, X. Gu, Q. Zeng, B. Lumbers and G. Li, *New J. Chem.*, 2024, **48**, 631.
- 87 Y. Qin, T. T. Yu, S. H. Deng, X. Y. Zhou, D. M. Lin, Q. Zhang, Z. Y. Jin, D. F. Zhang, Y. B. He, H. J. Qiu, L. H. He, F. Y. Kang, K. K. Li and T. Y. Zhang, *Nat. Commun.*, 2022, **13**, 3784.
- 88 J. Zhang, L. Xu, X. Yang, S. Guo, Y. Zhang, Y. Zhao, G. Wu and G. Li, *Angew. Chem. Inter. Ed.*, e202405641.
- 89 Q. Liang, A. Bieberle-Hütter and G. Brocks, *J. Phys. Chem. C*, 2022, **126**, 1337-1345.
- 90 Y. Hu, G. Luo, L. Wang, X. Liu, Y. Qu, Y. Zhou, F. Zhou, Z. Li, Y. Li, T. Yao, C. Xiong, B. Yang, Z. Yu and Y. Wu, *Adv. Energy Mater.*, 2020, **11**, 2002816.
- 91 Y. Yao, S. Hu, W. Chen, Z. Huang, W. Wei, T. Yao, R. Liu, K. Zang, X. Wang, G. Wu, W. Yuan, T. Yuan, B. Zhu, W. Liu, Z. Li, D. He, Z. Xue, Y. Wang, X. Zheng, J. Dong, C. Chang, Y. Chen, X. Hong, J. Luo, S. Wei, W. Li, P. Strasser, Y. Wu and Y. Li, *Nat. Catal.*, 2019, **2**, 304-313.
- 92 Z. L. Zhao, Q. Wang, X. Huang, Q. Feng, S. Gu, Z. Zhang, H. Xu, L. Zeng, M. Gu and H. Li, *Energy Environ. Sci.*, 2020, **13**, 5143-5151.
- 93 C. Hitz and A. Lasia, *J. Electroanal. Chem.*, 2001, **500**, 213-222.
- 94 G. Panomsuwan, N. Saito and T. Ishizaki, *ACS Appl Mater Interfaces*, 2016, **8**, 6962-6971.
- 95 Z. Li, M. Xu, J. Wang, Y. Zhang, W. Liu, X. Gu, Z. K. Han, W. Ye and G. Li, *Small*, 2024, 2400036.
- 96 X. Zhang, X. Zhu, S. Bo, C. Chen, M. Qiu, X. Wei, N. He, C. Xie, W. Chen, J. Zheng, P. Chen, S. P. Jiang, Y. Li, Q. Liu and S. Wang, *Nat. Commun.*, 2022, **13**, 5337.
- 97 P. Hildebrandt, M. Tsuboi and T. G. Spiro, *J. Phys. Chem.*, 1990, **94**, 2274-2279.
- 98 Y. Zhao, X. Zhang, N. Bodappa, W. Yang, Q. Liang, P. M. Radjenovica, Y. Wang, Y. Zhang, J. Dong, Z. Tian and J. Li, *Energy Environ. Sci.*, 2022, **15**, 3968-3977.
- 99 Z. Liu, Z. Qin, C. Cui, Z. Luo, B. Yang, Y. Jiang, C. Lai, Z. Wang, X. Wang, X. Fang, G. Li, F. Wang, C. Xiao and X. Yang, *Sci. China Chem.* 2022, **65**, 1196.
- 100 W. Zhang, Y. Zhou, W. Chen, T. Wang, Z. Qin, G. Li, Z. Ren, X. Yang, C. Zhou, *Chin. J. Chem. Phys.*, 2023, **36**, 249.



Data availability is not applicable to this article as no new data were created or analyzed in this study.

View Article Online
DOI: 10.1039/D4CC02722A

